# Nanoparticles in nematic liquid crystals: Interactions with nanochannels

Francisco R. Hung,[a] Brian T. Gettelfinger, Gary M. Koenig, Jr., Nicholas L. Abbott, and Juan J. de Pablo[b]
*Department of Chemical and Biological Engineering, University of Wisconsin, Madison, Wisconsin 53706-1691, USA*

(Received 29 March 2007; accepted 17 July 2007; published online 26 September 2007)

A mesoscale theory for the tensor order parameter **Q** is used to investigate the structures that arise when spherical nanoparticles are suspended in confined nematic liquid crystals (NLCs). The NLC is "sandwiched" between a wall and a small channel. The potential of mean force is determined between particles and the bottom of the channels or between several particles. Our results suggest that strong NLC-mediated interactions between the particles and the sidewalls of the channels, on the order of hundreds of $k_BT$, arise when the colloids are inside the channels. The magnitude of the channel-particle interactions is dictated by a combination of two factors, namely, the type of defect structures that develop when a nanoparticle is inside a channel, and the degree of ordering of the nematic in the region between the colloid and the nanochannel. The channel-particle interactions become stronger as the nanoparticle diameter becomes commensurate with the nanochannel width. Nanochannel geometry also affects the channel-particle interactions. Among the different geometries considered, a cylindrical channel seems to provide the strongest interactions. Our calculations suggest that small variations in geometry, such as removing the sharp edges of the channels, can lead to important reductions in channel-particle interactions. Our calculations for systems of several nanoparticles indicate that linear arrays of colloids with Saturn ring defects, which for some physical conditions are not stable in a bulk system, can be stabilized inside the nanochannels. These results suggest that nanochannels and NLCs could be used to direct the assembly of nanoparticles into ordered arrays with unusual morphologies. © *2007 American Institute of Physics*. [DOI: 10.1063/1.2770724]

## I. INTRODUCTION

Besides their traditional applications in displays, liquid crystals (LCs) have recently attracted attention for their potential uses in optical sensors. Recent experiments[1–6] and calculations[7,8] have demonstrated that the binding of chemicals, biomolecules, and viruses at solid-LC and liquid-LC functionalized interfaces perturbs the local ordering of the LC and triggers the formation of inhomogeneous textures. Due to the long-range order of the LCs, these inhomogeneities can be amplified over several length scales and detected using polarized light. Systems of particles immersed in liquid crystals also have potential applications for development of composites, nanostructured materials, and colloidal crystals.[9–15] The inclusion of colloids induces elastic distortions in the LC, giving rise to long-range interparticle interactions that can induce the formation of a number of ordered colloid structures. These LC-mediated interparticle interactions can be large, up to several thousands of $k_BT$, according to recent calculations[16–20] and experimental measurements[10,15] for colloids in nematic liquid crystals (NLCs). Such interactions are reversible and disappear when the LC is in the isotropic phase. The LC-mediated colloidal interactions also depend on the size and shape of the particles,[20] the local ordering of the molecules of LC at the surfaces of the colloids, and the alignment of the director field $\mathbf{n}(\mathbf{r})$ far away from the particles.

The response of a biosensor, or the structure of a microemulsion or suspension of particles in LCs, is dictated by the LC defects that arise around a collection of particles. The uniform alignment of a nematic is usually distorted by the inclusion of particles, due to the constraints imposed by the anchoring of the LC at the particles' surfaces. Topological defects are observed when these constraints impose conflicting orientations to the LC, giving rise to discontinuities in the director field $\mathbf{n}(\mathbf{r})$.[21] The LC defect core is characterized by strong biaxiality and a pronounced decrease in the scalar order parameter $S(\mathbf{r})$, which measures the degree of orientational order; a low value of $S(\mathbf{r})$ reflects the fact that the liquid crystal "melts" locally at the defect core.[21,22] Optimization of the applications mentioned above therefore requires a fundamental understanding of the structure and dynamics of topological defects around particles immersed in a LC, as well as the LC-induced interparticle interactions that arise due to elastic distortions.

Three types of defects are observed when a spherical particle is placed in a NLC: the dipole configuration (where the NLC forms a point defect known as a hyperbolic hedgehog),[9,23] the Saturn ring configuration (where the particle is surrounded by a disclination loop),[24,25] and the surface ring configuration (where the NLC forms two surface defects known as boojums).[23] They have been the focus of a

[a]Present address: Cain Department of Chemical Engineering, Louisiana State University, Baton Rouge, LA 70803, USA.
[b]Electronic mail: depablo@engr.wisc.edu

 

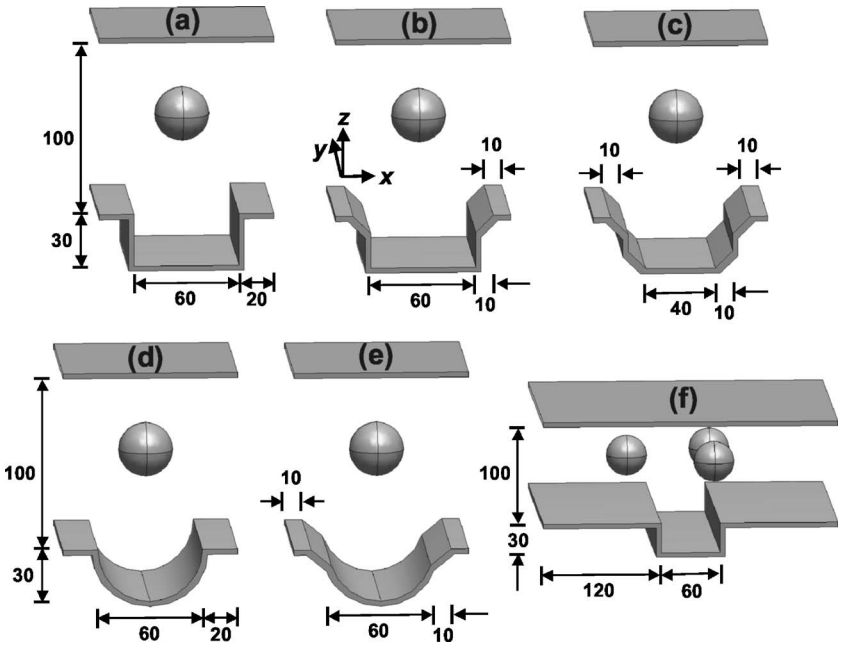


FIG. 1. Scheme of the different nanochannel geometries considered in this work: (a) rectangular, (b) rectangular with two straight cuts, (c) rectangular with four straight cuts, (d) cylindrical, (e) cylindrical with two straight cuts, and (f) rectangular nanochannel for a system of three nanoparticles. For all cases, the model systems consist of a wall and a nanochannel, "sandwiching" one or several spherical nanoparticles immersed in a nematic liquid crystal (NLC). All the dimensions are in nanometers. The total length of the system in the *y* direction is 100 nm for (a)–(e) and 300 nm for (f).

number of theoretical and numerical studies.[26–31] The dipole configuration was found to be stable for strong surface anchoring and micron-sized spherical particles. The Saturn ring configuration was predicted to become stable upon reduction of particle size, which was confirmed experimentally by the recent work of Völtz *et al.*[32] Magnetic and electric fields.[33] and confinement conditions[25,34] were also shown to stabilize a Saturn ring configuration. A surface ring defect is observed upon reduction of the surface anchoring strength.[29,30] Systems involving two spherical particles exhibiting Saturn ring (i.e., nanometer-sized particles) (Refs. 16–18) and hyperbolic hedgehog[35,36] defects have been recently examined using a mesoscale theory, where the NLC is described using the tensor order parameter $\mathbf{Q}(\mathbf{r})$. In the former series of studies, the predictions of the mesoscale theory were compared to those of molecular simulations, thereby providing a measure of the validity of the theory at nanometer length scales. In those calculations, a third disclination ring orthogonal to the original ones was observed between the two spheres at short separations.[16–18] Given the good agreement between the defect structures and the potentials of mean force obtained from Monte Carlo simulations and the mesoscale theory, the latter approach (which is computationally less expensive) was used to study the stability of arrays of three spherical nanoparticles immersed in a NLC,[19] and spherocylindrical nanoparticles in a NLC.[20] The continuum mesoscale theory approach was also used to study the structure and dynamics of a nematic in a two-dimensional (2D) representation of a liquid crystal sensor,[1,2] where chemicals or biomolecules (represented as spherical nanoparticles) can adsorb at the sensor walls.[7] Very recently, density functional theory has been used to study the structure of a LC, in its isotropic and nematic phase, around a cylindrical particle of infinite length.[37]

In this work, we use computer simulations to predict the behavior of systems of one or several nanoparticles in NLCs, when they are close to or confined in nanochannels of different geometries. Micron-sized channels have been used previously to elongate DNA molecules, as part of a recently proposed approach for genome analysis.[38,39] Very recently, Fernández-Nieves *et al.* used flow in microchannels to induce reversible changes in the topological defects of NLC droplets in water.[40] The aim of our work is to explore the use of NLCs and *nanochannels* to manipulate *nanoparticles* (as opposed to micron-sized channels and particles) and direct their assembly into controlled, ordered structures. Experimental work for these nanoscale systems is expected to face more difficulties as compared to their micron-sized counterparts. Therefore we turn to computer simulation as a way to explore and obtain rapid predictions of the behavior of systems of nanoparticles in NLCs close to nanochannels. Here we report numerical calculations for the LC defect structures that arise for such systems. A continuum mesoscale theory in terms of the tensor order parameter $\mathbf{Q}$ is used to model the nematic solvent. Systems containing one and three nanoparticles with strong homeotropic anchoring are considered. We also calculate the potential of mean force (PMF) for the different systems. The PMF gives the difference in free energy between two states, as a function of a specific degree of freedom of the system, namely, the minimum distance between a nanoparticle and the bottom of the nanochannel. The paper is organized as follows. In Sec. II we present a description of our model systems and details of the numerical methodology. Our results are presented and discussed in Sec. III. Section IV includes some concluding remarks and suggestions for future work.

## II. MODELS AND METHODS

### A. Details of the model systems

The model system considered in this work consists of a nanochannel and a wall, "sandwiching" one or several spherical nanoparticles immersed in a NLC. A schematic representation of the different nanochannel geometries consid-

ered in this work for one-particle systems is shown in Fig. 1. In all cases, the nanochannels exhibit a width of 60 nm, a depth of 30 nm, and the distance between the top wall and the bottom of the nanochannel is 130 nm. Spherical nanoparticles with diameters between $D=10$ nm and $D=50$ nm are considered. These particle diameters are given such that when the colloid is far away from the top wall and the nanochannel, a Saturn ring defect structure is formed by the NLC around the nanoparticle. All the surfaces present in the system (colloids, walls, and nanochannel) exhibit strong homeotropic anchoring conditions for the NLC. Such conditions can be easily achieved experimentally by coating the surfaces with a self-assembled monolayer of alkanethiols.[41] In the absence of particles, and away from the nanochannel, the system exhibits a homogeneous texture in which the director field $\mathbf{n}(\mathbf{r})$ is parallel to the $z$ axis. Strong variations in the director field, scalar order parameter, and topological defects are observed inside the nanochannels (particularly in the rectangular channel, Fig. 1) even when nanoparticles are not present, due to the conflicting orientations imposed to the nematic by the homeotropic anchoring conditions. The boundary conditions at the borders of the simulation box in the $x$ and $y$ directions are such that the director field $\mathbf{n}(\mathbf{r})$ is parallel to the $z$ axis. In all the systems studied in this work, the minimum distance between the surface of the particles and the borders of the simulation box in the $x$ and $y$ directions is always larger than 25 nm [equivalent to $1.45\xi$, where $\xi$ represents a characteristic length scale in our theory for spatial variations of $\mathbf{Q}$; see Eq. (7) below], and thus periodic boundary conditions were not required.

For one-particle systems, we considered different configurations where we changed the position of the nanoparticle along the $z$ axis, from a position where the particle is close to the top wall to a position where it is near the bottom of the nanochannel. The PMF and the defect structures were determined as a function of $d$, the minimum distance between the sphere and the bottom of the nanochannel. For systems containing three colloids, we computed the difference in free energies between several particle arrangements involving a rectangular nanochannel.

### B. Mesoscale theory for the nematic liquid crystal

The behavior of the NLC was modeled using a mesoscale theory for the tensor order parameter $\mathbf{Q}(\mathbf{r})$. In contrast to the director field $\mathbf{n}(\mathbf{r})$, $\mathbf{Q}(\mathbf{r})$ is free of divergences and discontinuities even at the disclination lines. The local values of the scalar order parameter $S(\mathbf{r})$ and the director $\mathbf{n}(\mathbf{r})$ can be obtained from $\mathbf{Q}$ through its largest eigenvalue $2S/3$ and its associated eigenvector, respectively.[21] In previous studies of spherical nanoparticles in a NLC,[16–18] it was shown that the results for potentials of mean force and defect structures obtained from this theory are in agreement with those from molecular simulations (where the NLC was represented as Gay-Berne ellipsoids), down to length scales comparable to the size of a LC molecule. This theory corresponds to a particular case of the Beris-Edwards formulation of the thermodynamics of fluids with internal microstructure.[42] In this formulation, the evolution of the tensor order parameter $\mathbf{Q}$ as a function of position $\mathbf{r}$ and time $t$ is determined by the functional derivative of the system free energy $F$ with respect to $\mathbf{Q}$,

$$\frac{\partial \mathbf{Q}}{\partial t} = -\frac{1}{\gamma}\left[\frac{\delta F}{\delta \mathbf{Q}} - \frac{1}{3}\mathrm{Tr}\left(\frac{\delta F}{\delta \mathbf{Q}}\right)\mathbf{I}\right]. \tag{1}$$

Here $\gamma$ is a kinetic coefficient associated with the rotational viscosity of the liquid crystal, and for simplicity it is assumed to be a constant. In this equation, it is assumed that $\delta F/\delta \mathbf{Q}$ has been symmetrized. The free energy $F$ of the liquid crystal includes three contributions given as follows:

$$F = \int d\mathbf{r} f_{\mathrm{LdG}}(\mathbf{r}) + \int d\mathbf{r} f_e(\mathbf{r}) + \oint dS f_s(\mathbf{r}). \tag{2}$$

The first term $f_{\mathrm{LdG}}$ represents a Landau–de Gennes expansion[21] describing the short-range interactions that drive the bulk isotropic-nematic phase transition,

$$f_{\mathrm{LdG}} = \frac{A}{2}\left(1-\frac{U}{3}\right)\mathrm{Tr}(\mathbf{Q}^2) - \frac{AU}{3}\mathrm{Tr}(\mathbf{Q}^3) + \frac{AU}{4}[\mathrm{Tr}(\mathbf{Q}^2)]^2. \tag{3}$$

The phenomenological coefficients $A$ and $U$ depend on the liquid crystal of interest. $A$ controls the energy scale of the model, whereas $U$ controls the value of the bulk scalar order parameter $S$,

$$S_{\mathrm{bulk}} = \frac{1}{4}\left(1+3\sqrt{1-\frac{8}{3U}}\right). \tag{4}$$

In this model, the system is isotropic for $0<U<2.7$ and nematic for $U>2.7$. The limits of metastability for the isotropic and nematic phases are $U=3$ and $8/3$, respectively. The third term in Eq. (2) represents the surface contribution to the free energy, and accounts for the liquid crystal anchoring at the surfaces. We only consider the case of strong homeotropic anchoring at all surfaces. In this limiting case, the prescribed perpendicular orientation of the liquid crystal at every surface must be satisfied, lest $f_s$ diverges. In our calculations, the homeotropic anchoring of the liquid crystal at every surface is enforced through the boundary conditions.

The second term in Eq. (2) describes the long-range elastic forces of the liquid crystal, and introduces a free energy penalty associated with gradients of the tensor order parameter field. For simplicity, in our calculations we have used the one-elastic-constant approximation,[21] where the splay, twist, and bend elastic constants $K_{11}$, $K_{22}$, and $K_{33}$ have a common value. In a previous simulation study for systems of spherocylindrical nanoparticles in nematic liquid crystals,[20] we obtained similar results for the defect structures and potentials of mean force when we used the one-elastic-constant approximation and a three-constant expression that is cubic in $\mathbf{Q}$ and its gradients.[42–44] The elastic free energy in the one-elastic-constant approximation takes the following form:

$$f_e = \frac{L_1}{2}\partial_k Q_{ij}\partial_k Q_{ij}. \tag{5}$$

In Eq. (5) $i,j,k \in x,y,z$, and the Einstein summation convention over repeated indexes is used. When the functional derivatives in Eq. (1) are evaluated with Eqs. (2), (3), and (5), the following partial differential equation for $\mathbf{Q}$ is obtained:

$$\frac{\partial Q_{ij}}{\partial t} = -\frac{1}{\gamma}\left\{A\left(1-\frac{U}{3}\right)Q_{ij} - AU \times\left[Q_{ik}Q_{kj} - \frac{\delta_{ij}}{3}Q_{kl}Q_{kl} - Q_{ij}(Q_{kl}Q_{kl})\right] - L_1\partial_k\partial_k Q_{ij}\right\}. \quad (6)$$

Equation (6) was solved numerically for all the three dimensional (3D) systems considered in this study. The values of the dimensionless parameters are $A=1$, $U=6$, $\gamma=400$, and $L_1=1$, corresponding to $S_{\text{bulk}}=0.81$. Given suitable scaling factors for pressure ($10^5$ Pa), length (10 nm), and time (1 ns), these parameters correspond to a material having an elastic constant $K=5$ pN (within the one-elastic-constant approximation) and an orientational viscosity of 0.04 Pa s. These values are representative of a low molecular-weight liquid crystal, such as 5CB. In addition, from a dimensional analysis one can obtain a characteristic length scale, or nematic coherence length, for spatial variations of $\mathbf{Q}$,[22]

$$\xi = \sqrt{18L_1/AU}, \quad (7)$$

which corresponds to $\xi=17.3$ nm for our numerical parameters.

Equation (6) was solved for the five independent components of $\mathbf{Q}$ ($Q_{xx}$, $Q_{yy}$, $Q_{xy}$, $Q_{xz}$, and $Q_{yz}$, since $\mathbf{Q}$ is traceless) using finite elements.[45] In order to solve the equations, we used the time-dependent algorithm DASPK, combined with the linear system solver GMRES and the incomplete LU preconditioner.[45] Equation (6) was solved for a sufficiently long time to observe negligible variations in the numerical solution with respect to time, which corresponds to finding the solution that minimizes the free energy [the right-hand side of Eq. (6)]. We performed three-dimensional simulations using unstructured meshes containing tetrahedral, linear Lagrange elements.[46] Different grid densities were used, and it was found that for the solutions to be independent of further mesh refinements, 59 346 and 72 852 finite elements were required in systems with one and three particles. The mesh was significantly finer in the immediate vicinity of the walls and the nanoparticles, where important curvature effects and strong variations in $\mathbf{Q}$ are present. The minimum length size of the finite elements was approximately $1.1\times10^{-3}$ nm. For the smallest particle diameter considered ($D=10$ nm), our finest grid size corresponds to $1.1\times10^{-4}D$, which is comparable to those reported by Fukuda *et al.*[31] in their adaptive mesh refinement scheme. The initial conditions of $\mathbf{Q}$ in our simulations are such that the director $\mathbf{n}$ is initially aligned along the $z$ direction, and the scalar order parameter $S$ was initially fixed to the equilibrium value $S_{\text{bulk}}=0.81$ [Eq. (4)]. The scalar order parameter at the nanoparticles' surface was also set to $S=S_{\text{bulk}}=0.81$. Different methods are available to depict the NLC defect structures (the regions where the nematic director field becomes discontinuous).[47–50] In this work, we follow previous literature studies[16–20] and adopt the contour $S=0.30$ to visualize defects in 3D, since it is approximately the smallest value of scalar order parameter for a stable bulk nematic in our particular model.[22,42] The free energy values used in the computation of the potential of mean force were determined by numerical integration of Eqs. (2), (3), and (5) over the volume of the system.

## III. RESULTS AND DISCUSSION

### A. Effect of the ratio particle diameter/nanochannel width

Our first aim is to determine the defect structures and the potential of mean force that arise when a spherical nanoparticle, immersed in a nematic liquid crystal, interacts with a rectangular nanochannel of width 60 nm and depth 30 nm. Different colloid diameters were considered ($D=10$, 20, 30, 40, and 50 nm). All surfaces induce homeotropic anchoring to the nematic, and the director field far away from the surfaces is parallel to the $z$ axis. We consider different configurations, where we changed the position of the nanoparticle gradually along the $z$ axis, from the top wall to the bottom of the nanochannel. The PMF was determined as a function of the minimum distance $d$ between the colloid and the bottom of the nanochannel. For each of these distances, the PMF was calculated as the difference in free energy with respect to that observed when the particle's center is 50 nm from the top wall and 80 nm from the bottom of the nanochannel, i.e., a situation where the colloid is far away from both the top wall and the bottom of the nanochannel. In most of the cases, the $x$ and $y$ coordinates of the colloid are such that the particle is equidistant from the sidewalls of the nanochannel; however, we considered one case where a nanoparticle of $D=10$ nm is closer to one of the sidewalls of the channel. Results for the PMF are presented in Fig. 2.

We first discuss the cases where the nanoparticle is equidistant from the sidewalls of the channel. For a small particle of $D=10$ nm, there is almost no effect on the total PMF curve [Fig. 2(a)], and we observe a small repulsion when the particle is close to the top wall and the bottom of the channel. This repulsion is due to distortions in the director field of the nematic caused by the curvature effects at the surface of the particle and the homeotropic anchoring conditions at the walls and the sphere. These repulsion effects have been observed in a previous study that considered a system of a colloid in a NLC close to a flat wall, using both Monte Carlo simulations and theory.[16] In Figs. 2(b) and 2(c) we depict the Landau–de Gennes (LdG) and elastic contributions to the total PMF. For $D=10$ nm, the LdG and elastic PMF show a maximum and a minimum, respectively, of a few $k_BT$ occurring at the same value of $d$, and therefore they compensate each other so that almost no variation is observed in the total PMF.

As the diameter of the nanoparticle increases, several effects are apparent in the curves for the total PMF [Fig. 2(a)]. First, the magnitude of the repulsion as the particle is close to the top wall and the bottom of the nanochannel increases, since the larger particle sizes cause more distortions in the director field as the colloid gets closer to the walls. Second, the curves for the total PMF show a decrease as the particle approaches the nanochannel, reaching minima of $\sim 56k_BT$($D=20$ nm), $\sim 165k_BT$($D=30$ nm), $\sim 315k_BT$($D=40$ nm), and $\sim 410k_BT$($D=50$ nm). Such strong interactions arise because the Saturn ring defects around the nano-

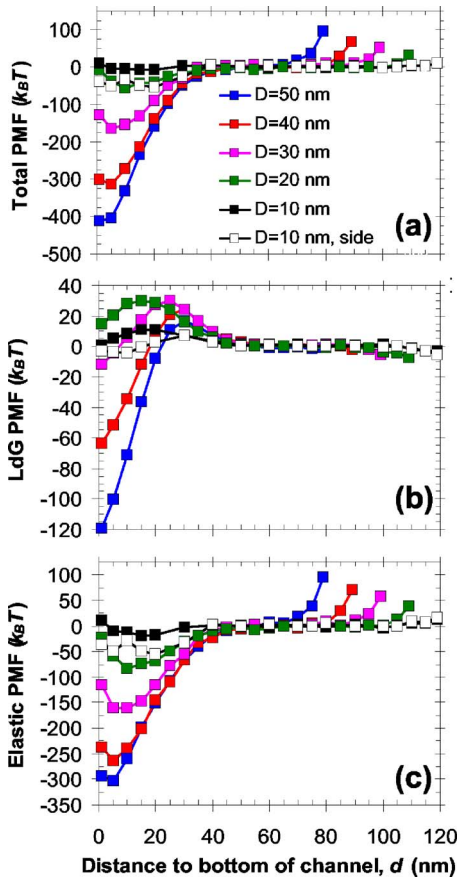


FIG. 2. (Color online) Potential of mean force (PMF) as a function of the minimum distance between one nanoparticle and the bottom of a rectangular nanochannel for different colloid diameters: (a) total PMF, (b) Landau–de Gennes contribution to the total PMF, and (c) elastic contribution to the total PMF.

particles interact and fuse with the NLC defects at the sides of the nanochannel, leading to important reductions in the total area of LC defects. In Fig. 3, we show visualizations of the defect structures observed for nanoparticles of $D=30$ and 50 nm, observed at different distances between the colloids and the bottom of the nanochannel. When the nanoparticle is far from both the top wall and the bottom of the nanochannel [Figs. 3(a) and 3(d)], a Saturn ring defect structure is formed by the nematic around the colloid, and the sidewalls of the nanochannel are also covered by defect structures. As a small colloid ($D=10$ nm) approaches the nanochannel, there is no significant interaction between the cores of the NLC defects around the particle and the sidewalls, and therefore no significant changes are observed in the PMF curves (Fig. 2). However, when a larger colloid ($D=30$ nm) approaches the nanochannel [Figs. 3(a)–3(c)], the defect structures around the nanoparticle and the sidewalls of the channel start to interact by extending toward each other and becoming more and more distorted until they eventually fuse together [Fig 3(b)]. This configuration corresponds to the maxima in the LdG PMF curves [Fig. 2(b)], where the size of the defect structures (and therefore the amount of nematic that melts in the defect core) reaches a maximum. From Fig. 2(b), it is also apparent that the maxima in the LdG PMF curves decrease and move to larger values of $d$, as the diameter of the nanoparticle increases.

Further reductions in $d$ lead to smaller defect structures consisting of an incomplete Saturn ring fused with the defects on the sidewalls of the channel [Fig. 3(c), which corresponds to the minima of the total and elastic PMF curves, Figs. 2(a) and 2(c)]. In this configuration, the NLC in the region between the nanoparticles and the sidewalls of the

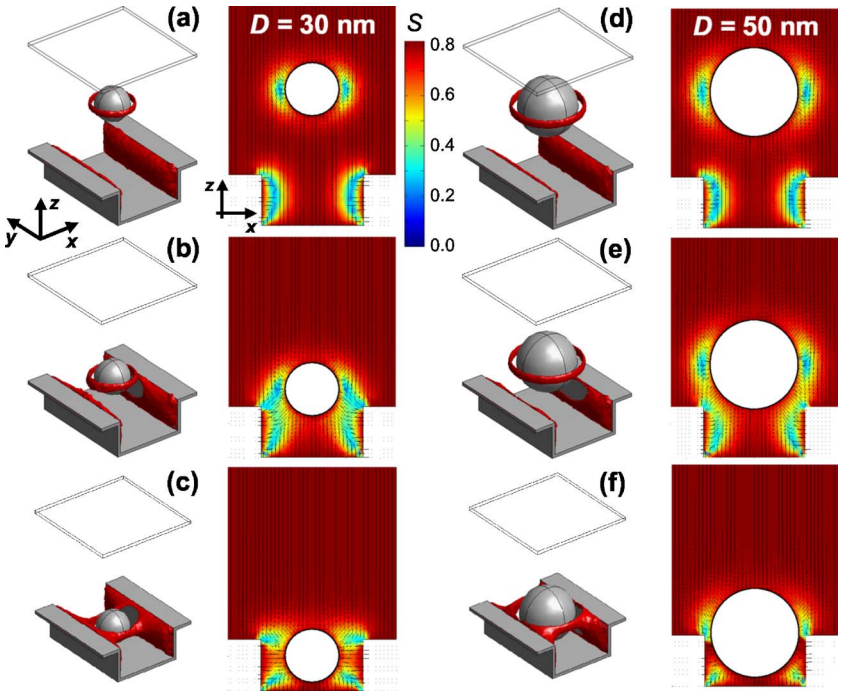


FIG. 3. (Color online) 3D visualizations of the NLC defect structures (represented as the contour $S=0.30$ in red) and 2D contour maps of the scalar order parameter $S$, superimposed with the director field $\mathbf{n}$ in the $x$-$z$ plane, for one nanoparticle with $D=30$ nm (a)–(c) and $D=50$ nm (d)–(f), at different values of $d$: (a) $d=65$ nm (far apart from both the top wall and the nanochannel), (b) $d=25$ nm [the maximum in the LdG PMF, Fig. 2(b)], (c) $d=5$ nm [the minimum in the total and elastic PMF, Figs. 2(a) and 2(c)], (d) $d=55$ nm (far apart from both the top wall and the nanochannel), (e) $d=30$ nm [the maximum in the LdG PMF, Fig. 2(b)], and (f) $d=5$ nm [the minimum in the total and elastic PMF, Figs. 2(a) and 2(c)]. For all cases, the particle is equidistant from the sidewalls of the channel.

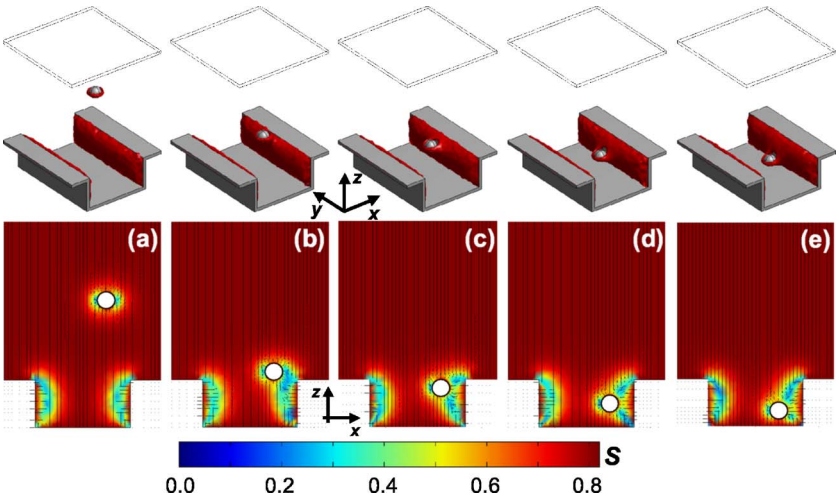


FIG. 4. (Color online) 3D visualizations of the NLC defect structures (represented as the contour $S=0.30$ in red, top) and 2D contour maps of the scalar order parameter $S$, superimposed with the director field $\mathbf{n}$ in the $x$-$z$ plane (bottom), for one nanoparticle with $D=10$ nm at (a) $d=75$ nm (far apart from both the top wall and the nanochannel), (b) $d=30$ nm [the maximum in the LdG PMF, Fig. 2(b)], (c) $d=20$ nm [the first minimum in the total and elastic PMF, Figs. 2(a) and 2(c)], (d) $d=10$ nm [the minimum in the LdG PMF, Fig. 2(b)], and (e) $d=5$ nm [the second minimum in the total and elastic PMF, Figs. 2(a) and 2(c)]. The particle is closer to one of the sidewalls of the channel. (see text)

channel becomes highly ordered [Fig. 3(c)]. Here, the particle is close enough to the sidewalls of the channel, and thus the local homeotropic anchoring persists in the interparticle space, and a "bridge" of director lines forms [Fig. 3(c)]. Microscopically, this corresponds to a few layers of liquid crystal molecules connecting the nanoparticle and the sidewalls of the nanochannel, in analogy to what was observed in the interparticle regions between the spherical[17–19] and spherocylindrical[20] colloids immersed in NLCs. These effects are more pronounced for a particle that has a size ($D=50$ nm) comparable to that of the nanochannel (width $=60$ nm) [Figs. 3(d)–3(f)]. A larger particle surrounded by a Saturn ring exhibits a larger amount of energy in the defect cores, since the free energy tends to increase with particle size.[31] As a particle enters the nanochannel and reaches the minimum of the PMF curve, the reduction in the total area of NLC defects increases with particle size [compare Figs. 3(c) and 3(f)]. In addition, the nematic in the region between the nanoparticle and the sidewalls of the channel becomes more ordered, as compared to what was observed for the case of $D=30$ nm [Figs. 3(a)–3(c)]. As a result, the interactions between a particle of $D=50$ nm and the nanochannel are stronger ($\sim 410 k_B T$) when compared to those observed for a colloid of $D=30$ nm ($\sim 165 k_B T$).

So far we have considered cases where the nanoparticle is equidistant from the sidewalls of the channel. Results for the PMF for a small nanoparticle ($D=10$ nm) when it is closer to one of the sidewalls of the nanochannel are presented in Fig. 2, and visualizations of the defect structures are depicted in Fig. 4. In this case, the minimum distance along the $x$ axis between the particle and the nearest sidewall of the nanochannel was set at 10 nm. The total PMF for this case shows two minima at $d=20$ nm and $d=5$ nm, and a local maximum at $d=10$ nm; these features are also observed in the elastic PMF. The LdG PMF for this case exhibits one maximum at $d=30$ nm and a minimum at $d=10$ nm. The two minima and the local maximum in the PMF are caused by the fact that the Saturn ring defect around the nanoparticle interacts with the defects at the sidewalls of the channel which have a nonuniform thickness (Fig. 4). Note that the minimum of $\sim 50 k_B T$ observed in the total PMF is comparable to the interactions observed for the case of a larger nanoparticle ($D=20$ nm) interacting with both sidewalls of the nanochannel.

### B. Effect of nanochannel geometry

The experimental fabrication of perfectly rectangular nanoscale channels can be challenging. We therefore consider in this section a variety of channel geometries. We present results for the defect structures and the potential of mean force, for a system of one spherical nanoparticle immersed in a NLC, interacting with rectangular and cylindrical nanochannels that include several variations: (1) rectangular (same geometry analyzed in the previous section), (2) cylindrical, (3) rectangular with two "straight" cuts, (4) rectangular with four straight cuts, and (5) cylindrical with two straight cuts. These different nanochannel geometries are represented in Fig. 1. In all cases, the nanochannel has a width and depth of 60 and 30 nm, respectively; and the cuts in the nanochannel have a width of 10 nm each (Fig. 1). Two particle diameters are considered, $D=30$ nm and $D=50$ nm, and in all cases, the particle is equidistant from the sidewalls of the nanochannel. Results for the PMF are presented in Fig. 5.

In each of the nanochannel geometries considered, it is apparent that the minima in both the total and elastic PMF become more negative [Figs. 5(a) and 5(c)] as the diameter of the nanoparticle increases. In addition, the maxima in the LdG curves [Fig. 5(b)] decrease and move to larger values of $d$, in each nanochannel geometry, as the diameter of the nanoparticle increases. These effects were also discussed in the previous section for rectangular channels. Among the different nanochannel geometries, two groups of curves can be observed in the total PMF for $D=50$ nm [Fig. 5(a)], where the strongest channel-particle interactions are observed for the cylindrical and rectangular nanochannels, followed by the channels with straight cuts. For $D=30$ nm, the strongest channel-particle interactions are observed for the cylindrical nanochannel, followed by the rectangular channel, the cylindrical, and the rectangular channels with two straight cuts, and finally, the weakest channel-particle interactions are observed for the rectangular channels with four straight cuts

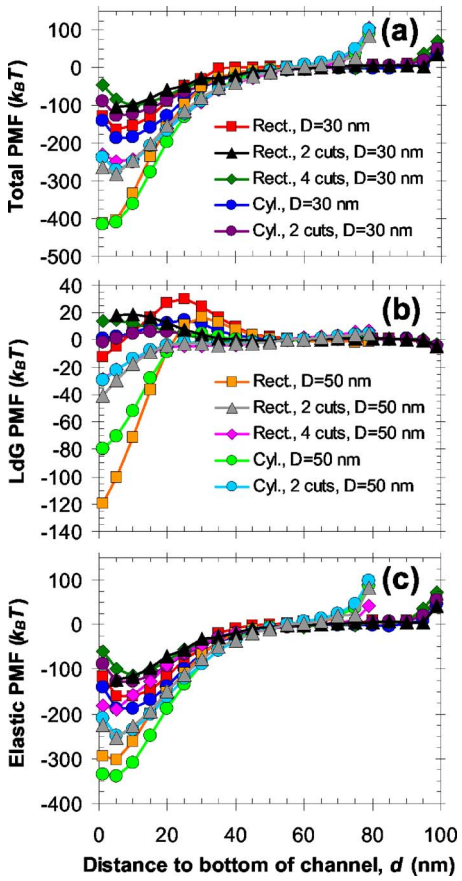


FIG. 5. (Color online) Potential of mean force (PMF) as a function of the minimum distance between one nanoparticle and the bottom of a nanochannel for different channel geometries and two colloid diameters, $D=30$ and 50 nm: (a) total PMF, (b) Landau–de Gennes contribution to the total PMF, and (c) elastic contribution to the total PMF.

[Fig. 5(a)]. In the LdG PMF [Fig. 5(b)], the largest maximum is observed for the rectangular nanochannel. Maxima of $5-30k_BT$ are present for $D=30$ nm in the LdG PMF for all the nanochannel geometries considered; however, these maxima decrease and in some cases disappear for a 50 nm nanoparticle.

In Figs. 6 and 7 we present 2D and 3D visualizations of the defect structures observed when the nanoparticle is close to the top wall, and at the minima of the total PMF curves [Fig. 5(a)], for the different nanochannel geometries considered above. Different LC defect structures form on the sidewalls of the channels in the absence of particles. As mentioned before, the sidewalls of a rectangular nanochannel are covered by a LC that exhibits strong variations in the director field and scalar order parameter [$S$ ranges from 0 to 0.82 inside the channel, Figs. 6(a) and 7(a)]. Elimination of the sharp edges in a rectangular channel reduces the variations in $\mathbf{n}(\mathbf{r})$ and $S(\mathbf{r})$. A smaller area of the sidewalls of a rectangular nanochannel with two straight cuts is covered by a LC with $S\sim 0.3$ [Figs. 6(b) and 7(b)], and no regions of $S\sim 0.3$ are observed inside a rectangular channel with four straight cuts [Figs. 6(c) and 7(c)]. For cylindrical channels, the regions of $S\sim 0.3$ are observed close to the sharp edges of the nanochannel [Figs. 6(d) and 7(d)]. Removing the sharp edges eliminates these regions, and smooth variations in $\mathbf{n}(\mathbf{r})$ and $S(\mathbf{r})$ are observed inside a cylindrical nanochannel with two straight cuts [Figs. 6(e) and 7(e)].

As discussed earlier, the magnitude of the PMF minima is dictated by a combination of two factors: (1) how much the total surface of the NLC defect cores is reduced when the nanoparticle is inside the channels (i.e., by comparing the size of the blue regions in the 2D visualizations, when the particle is far away and inside the channels), and (2) how ordered the nematic is in the region between the colloid and the nanochannel (i.e., how high the value of $S$ is in this specific region). From Figs. 6 and 7, it is clear that these effects are more important for a nanoparticle of $D=50$ nm in the cylindrical and rectangular nanochannels, and explain the magnitude of the different total PMF minima observed in Fig. 5(a). Our results suggest that a cylindrical channel provides the strongest channel-particle interactions. Nevertheless, as the ratio between the nanoparticle diameter and the nanochannel width increases, a rectangular and a cylindrical nanochannel seem to exhibit similar channel-particle interactions. Our results also suggest that small variations in the geometry of the channels, such as small cuts removing their sharp edges, lead to important changes in the channel-particle interactions. As an example, the difference in the total PMF minima between a nanoparticle of $D=50$ nm inside a rectangular nanochannel and a rectangular channel with four straight cuts represents 40% of the PMF minimum.

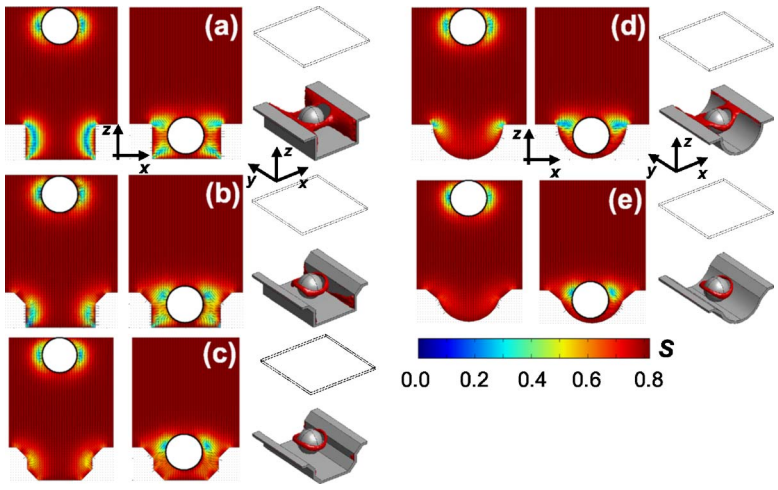


FIG. 6. (Color online) 2D contour maps of the scalar order parameter $S$, superimposed with the director field $\mathbf{n}$ in the $x$-$z$ plane, when a nanoparticle of $D=30$ nm is close to the top wall (left), and when the particle is inside the nanochannel (at the minima of the total PMF, center). For the latter situation, 3D visualizations of the NLC defect structures are also depicted (represented as the contour $S=0.30$ in red, right). Different nanochannel geometries are represented as follows: (a) rectangular, (b) rectangular with two cuts, (c) rectangular with four cuts, (d) cylindrical, and (e) cylindrical with two cuts. The particle is always equidistant from the sidewalls of the channel.

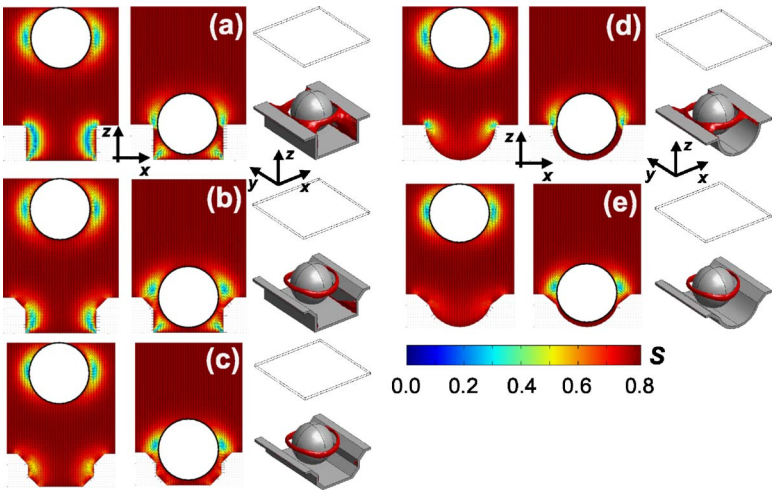


FIG. 7. (Color online) 2D contour maps of the scalar order parameter $S$, superimposed with the director field $\mathbf{n}$ in the $x$-$z$ plane, when a nanoparticle of $D=50$ nm is close to the top wall (left), and when the particle is inside the nanochannel (at the minima of the total PMF, center). For the latter situation, 3D visualizations of the NLC defect structures are also depicted (represented as the contour $S=0.30$ in red, right). Different nanochannel geometries are represented as follows: (a) rectangular, (b) rectangular with two cuts, (c) rectangular with four cuts, (d) cylindrical, and (e) cylindrical with two cuts. The particle is always equidistant from the sidewalls of the channel.

### C. Systems with several nanoparticles

We now consider the structures that arise when three nanoparticles are immersed in a NLC, and are confined between a wall and a rectangular nanochannel. We consider nanoparticles of $D=40$ nm, a nanochannel with width 60 nm and depth 30 nm, and a distance between the top wall and the bottom of the nanochannel of 130 nm (Fig. 1). The far-field director $\mathbf{n}(\mathbf{r})$ is parallel to the $z$ axis. Four different particle arrays are examined: (a) nanoparticles are far apart from the nanochannel, the top wall, and each other (minimum interparticle distance $l=60$ nm); (b) nanoparticles are close together ($l=5$ nm) forming a triangular array, and far apart from the nanochannel and the top wall; (c) nanoparticles are inside the nanochannel but far apart from each other ($l=60$ nm); and (d) nanoparticles are inside the nanochannel and close together ($l=5$ nm), forming a linear array. These four cases are depicted in Fig. 8, along with the free energy differences observed between the different particle arrays.

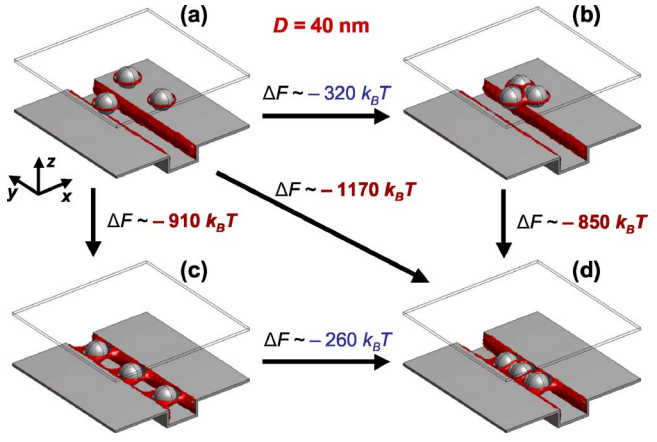


FIG. 8. (Color online) 3D visualizations of the NLC defect structures (represented as the contour $S=0.30$ in red) for different arrays of three nanoparticles with $D=40$ nm in a NLC "sandwiched" between a wall and a rectangular nanochannel: (a) nanoparticles are far apart from the nanochannel, the top wall, and each other (minimum interparticle distance $l=60$ nm); (b) nanoparticles are close together forming a triangular array ($l=5$ nm), and far apart from the nanochannel and the top wall; (c) nanoparticles are inside the nanochannel but far apart from each other ($l=60$ nm); and (d) nanoparticles are inside the nanochannel and close together ($l=5$ nm), forming a linear array.

Previous theoretical work has demonstrated that, for a bulk system of three nanoparticles in the $x$-$y$ plane suspended in a NLC where the far-field director $\mathbf{n}(\mathbf{r})$ is parallel to the $z$ axis, a triangular array is more stable than a linear array of colloids.[19] Our results indicate that the difference in free energy between particle arrays (a) and (b) is on the order of $320k_BT$ (Fig. 8). Our calculations also indicate that very strong interactions can be observed for linear arrays of nanoparticles inside rectangular nanochannels. The differences in free energy between arrays (a) and (c) and between arrays (a) and (d) are on the order of $910k_BT$ and $1170k_BT$, respectively. The differences in free energy between particle arrays (c) and (d) and (b) and (d) are on the order of $260k_BT$ and $850k_BT$, respectively. These very strong interactions can stabilize linear arrays of nanoparticles, which otherwise would not be stable in a bulk system with similar conditions of LC anchoring at the surfaces and far-field director alignment.

## IV. CONCLUDING REMARKS

We have studied the defect structures and potential of mean force (PMF) that arise when spherical nanoparticles in a nematic liquid crystal (NLC) are confined between a wall and a nanochannel. Our results suggest that strong NLC-mediated interactions arise between the particles and the sidewalls of the nanochannel. The channel-particle interactions are strongly influenced by the ratio of the nanoparticle diameter to the nanochannel width. The interactions range from a few $k_BT$ for a relatively small colloid to $400k_BT$ for the case of a nanoparticle with a diameter comparable to the nanochannel width. Our results indicate that nanochannel geometry also affects the channel-particle interactions. Among the different geometries considered, a cylindrical channel provides the strongest interactions with a particle; however, as the ratio of nanoparticle diameter to nanochannel width increases, a rectangular and a cylindrical nanochannel exhibit similar interactions with the particles. Our calculations suggest that small variations in the geometry of the channels, such as small cuts removing the sharp edges of the channels, lead to important changes in the channel-particle interactions

(up to 40% of the PMF minima observed for nanochannels with sharp edges). We believe that other geometry variables, such as the nanochannel depth, will also affect the channel-particle interactions. For all these systems, we propose that the magnitude of the channel-particle interactions is dictated by a combination of two factors: (1) how much the total surface of the NLC defect cores (which form around the nanoparticle and the sidewalls of the nanochannels) is reduced when the nanoparticle is inside the channels, and (2) the degree of ordering of the nematic in the region between the colloid and the nanochannel. Finally, our calculations for systems of several nanoparticles indicate that linear arrays of colloids inside the channels can exhibit particularly strong interactions with the sidewalls. These strong interactions can stabilize linear arrays of particles, which otherwise would not be stable in a bulk system with similar conditions of LC anchoring at the surfaces and far-field director alignment. Our findings are consistent with the results of Silvestre *et al.*,[51] who determined that an individual colloidal disk in a 2D nematic exhibits an attractive interaction towards a cavity with shape and size similar to those of the disk.

Our simulation results suggest that nanochannels could be used to direct the assembly of spherical nanoparticles into ordered, controlled arrays, for applications related to nanocomposites, nanostructured materials, colloidal crystals, photonics, etc. Nanochannels could also be used to separate particles of different sizes. Colloidal crystals with unusual structures could also be obtained by using channels and particles of asymmetric shapes (spherocylindrical, cubic, etc.) immersed in LCs. On the other hand, the strong LC defect-mediated channel-particle interactions determined in our calculations indicate that dynamics will play a significant role in directing the assembly of these systems of nanoparticles in LCs and nanochannels. Therefore, dynamical simulations[52–54] of these systems, where we follow the motion and reorganization of the particles and the nematic liquid crystal in different geometries, could allow us to determine, for example, how likely the particles are to reorganize between configurations similar to those shown in Fig. 8. These calculations could also provide useful insights into the actual mechanisms of self-assembly. These simulations are beyond the scope of the work presented here, and will be the subject of our future studies. Experiments are also currently underway to determine the validity of the predictions put forth in this work.

## ACKNOWLEDGMENTS

The authors are grateful to Orlando Guzmán for helpful discussions. This work was supported by the University of Wisconsin Nanoscale Science and Engineering Center (NSEC) on Templated Synthesis and Assembly at the Nanoscale (Research Thrust 3, Driven Nano-Fluidic Self-Assembly of Colloids and Macromolecules).

[1] V. K. Gupta, J. J. Skaife, T. B. Dubrovsky, and N. L. Abbott, Science **279**, 2077 (1998).
[2] R. R. Shah and N. L. Abbott, Science **293**, 1296 (2001).
[3] J. M. Brake, M. K. Daschner, Y. Y. Luk, and N. L. Abbott, Science **302**, 2094 (2003).
[4] S. V. Shiyanovskii, T. Schneider, I. I. Smalyukh, T. Ishikawa, G. D. Niehaus, K. J. Doane, C. J. Woolverton, and O. D. Lavrentovich, Phys. Rev. E **71**, 020702(R) (2005).
[5] C.-H. Jang, L.-L. Cheng, C. W. Olsen, and N. L. Abbott, Nano Lett. **6**, 1053 (2006).
[6] E. Tjipto, K. D. Cadwell, J. F. Quinn, A. P. R. Johnston, N. L. Abbott, and F. Caruso, Nano Lett. **6**, 2243 (2006).
[7] S. Grollau, O. Guzmán, N. L. Abbott, and J. J. de Pablo, J. Chem. Phys. **122**, 024703 (2005); O. Guzmán, N. L. Abbott, and J. J. de Pablo, *ibid.* **122**, 184711 (2005).
[8] D. K. Hwang and A. D. Rey, J. Chem. Phys. **125**, 174902 (2006).
[9] P. Poulin, H. Stark, T. C. Lubensky, and D. A. Weitz, Science **275**, 1770 (1997).
[10] P. Poulin, V. Cabuil, and D. A. Weitz, Phys. Rev. Lett. **79**, 4862 (1997).
[11] J. C. Loudet, P. Barois, and P. Poulin, Nature (London) **407**, 611 (2000).
[12] I. I. Smalyukh, S. Chernyshuk, B. I. Lev, A. B. Nych, U. Ognysta, V. G. Nazarenko, and O. D. Lavrentovich, Phys. Rev. Lett. **93**, 117801 (2004).
[13] J. C. Loudet, P. Barois, P. Auroy, P. Keller, H. Richard, and P. Poulin, Langmuir **20**, 11336 (2004).
[14] I. I. Smalyukh, O. D. Lavrentovich, A. N. Kuzmin, A. V. Kachynski, and P. N. Prasad, Phys. Rev. Lett. **95**, 157801 (2005).
[15] I. Muševič, M. Škarabot, U. Tkalec, M. Ravnik, and S. Žumer, Science **313**, 954 (2006).
[16] S. Grollau, E. B. Kim, O. Guzmán, N. L. Abbott, and J. J. de Pablo, J. Chem. Phys. **119**, 2444 (2003).
[17] O. Guzmán, E. B. Kim, S. Grollau, N. L. Abbott, and J. J. de Pablo, Phys. Rev. Lett. **91**, 235507 (2003).
[18] E. B. Kim, O. Guzmán, S. Grollau, N. L. Abbott, and J. J. de Pablo, J. Chem. Phys. **121**, 1949 (2004).
[19] O. Guzmán, N. L. Abbott, and J. J. de Pablo, J. Polym. Sci., Part B: Polym. Phys. **43**, 1033 (2005).
[20] F. R. Hung, O. Guzmán, B. T. Gettelfinger, N. L. Abbott, and J. J. de Pablo, Phys. Rev. E **74**, 011711 (2006).
[21] P. G. de Gennes and J. Prost, *The Physics of Liquid Crystals* (Clarendon, Oxford, 1993).
[22] N. Schopohl and T. J. Sluckin, Phys. Rev. Lett. **59**, 2582 (1987).
[23] P. Poulin and D. A. Weitz, Phys. Rev. E **57**, 626 (1998).
[24] O. Mondain-Monval, J. C. Dedieu, T. Gulik-Krzywicki, and P. Poulin, Eur. Phys. J. B **12**, 167 (1999).
[25] Y. Gu and N. L. Abbott, Phys. Rev. Lett. **85**, 4719 (2000).
[26] R. W. Ruhwandl and E. M. Terentjev, Phys. Rev. E **55**, 2958 (1997).
[27] R. W. Ruhwandl and E. M. Terentjev, Phys. Rev. E **56**, 5561 (1997).
[28] T. C. Lubensky, D. Pettey, N. Currier, and H. Stark, Phys. Rev. E **57**, 610 (1998).
[29] H. Stark, Eur. Phys. J. B **10**, 311 (1999).
[30] H. Stark, Phys. Rep. **351**, 387 (2000).
[31] J. Fukuda, M. Yoneya, and H. Yokoyama, Eur. Phys. J. E **13**, 87 (2004).
[32] C. Völtz, Y. Maeda, Y. Tabe, and H. Yokoyama, Phys. Rev. Lett. **97**, 227801 (2006).
[33] J. C. Loudet and P. Poulin, Phys. Rev. Lett. **87**, 165503 (2001).
[34] S. Grollau, N. L. Abbott, and J. J. de Pablo, Phys. Rev. E **67**, 011702 (2003).
[35] J. Fukuda, H. Stark, M. Yoneya, and H. Yokoyama, Phys. Rev. E **69**, 041706 (2004).
[36] J. Fukuda and H. Yokoyama, Phys. Rev. Lett. **94**, 148301 (2005).
[37] D. L. Cheung and M. P. Allen, Phys. Rev. E **74**, 021701 (2006).
[38] Y.-L. Chen, M. D. Graham, J. J. de Pablo, K. Jo, and D. C. Schwartz, Macromolecules **38**, 6680 (2005).
[39] K. Jo, D. M. Dhingra, T. Odijk, J. J. de Pablo, M. D. Graham, R. Runnheim, D. Forrest, and D. C. Schwartz, Proc. Natl. Acad. Sci. U.S.A. **104**, 2673 (2007).
[40] A. Fernández-Nieves, D. R. Link, M. Márquez, and D. A. Weitz, Phys. Rev. Lett. **98**, 087801 (2007).
[41] V. K. Gupta and N. L. Abbott, Science **276**, 1533 (1997).
[42] A. N. Beris and B. J. Edwards, *Thermodynamics of Flowing Systems with Internal Microstructure* (Oxford University Press, New York, 1994).
[43] B. J. Edwards and A. N. Beris, J. Rheol. **33**, 1189 (1989).
[44] B. J. Edwards, A. N. Beris, and M. Grmela, J. Non-Newtonian Fluid Mech. **35**, 51 (1990).
[45] COMSOL Multiphysics™, Version 3.2 User's Guide, COMSOL, Inc., Burlington, MA, 2005, and references therein (http://www.comsol.com).
[46] For the case of Eq. (6), the elastic term $L_1\partial_k\partial_k Q_{ij}$ and the Landau–de Gennes terms were included as part of the diffusive flux ($c$) and source ($f$) terms, respectively, of the coefficient PDE form of COMSOL Mult-

iphysics™. The models were created, executed, and saved as a MATLAB® M-file.
[47] S. Kralj, E. G. Virga, and S. Žumer, Phys. Rev. E **60**, 1858 (1999).
[48] S. Kralj and E. G. Virga, J. Phys. A **34**, 829 (2001).
[49] S. Kralj and E. G. Virga, Phys. Rev. E **67**, 021703 (2002).
[50] A. C. Callan-Jones, R. A. Pelcovits, V. A. Slavin, S. Zhang, D. H. Laidlaw, and G. B. Loriot, Phys. Rev. E **74**, 061701 (2006).
[51] N. M. Silvestre, P. Patrício, and M. M. Telo da Gama, Phys. Rev. E **69**, 061402 (2004).
[52] R. Yamamoto, Phys. Rev. Lett. **87**, 075502 (2001); R. Yamamoto, Y. Nakayama, and K. Kim, J. Phys.: Condens. Matter **16**, S1945 (2004).
[53] T. Araki and H. Tanaka, Phys. Rev. Lett. **97**, 127801 (2006).
[54] N. Sulaiman, D. Marenduzzo, and J. M. Yeomans, Phys. Rev. E **74**, 041708 (2006).